Chapter 6

SCANNING ELECTRON MICROSCOPY WITH POLARIZATION ANALYSIS (SEMPA) AND ITS APPLICATIONS

John Unguris
Electron Physics Group
National Institute of Standards and Technology
Gaithersburg, Maryland 20899-8412

6.1 Introduction

Scanning Electron Microscopy with Polarization Analysis (SEMPA) is a technique for directly imaging the magnetic microstructure of surfaces and thin films. SEMPA relies on the fact that secondary electrons emitted from a magnetic sample in a Scanning Electron Microscope (SEM) have a spin polarization which reflects the net spin density in the material. This spin density, in turn, is directly related to the magnetization of the material. By measuring the secondary electron spin polarization, SEMPA can be used for direct, high resolution imaging of the direction and relative magnitude of a sample's magnetization, in the same way that a SEM can be used to image topography by measuring the secondary electron intensity.

The SEMPA technique has evolved from measurements over the past few decades in which various conventional electron spectroscopies were combined with electron spin sensitivity to investigate the magnetic properties of surfaces and thin films. Several reviews of this early work are available [1, 2, 3, 4]. SEMPA microscopes, also sometimes referred to as spin-polarized electron microscopes (spin-SEMs), made their initial appearance in the mid 1980s [5, 6, 7]. Several reviews of the SEMPA technique and instrumentation have appeared since then [8, 9, 10, 11].

SEMPA is one of several methods used for imaging magnetic microstructure. Since each method has its own particular strengths and drawbacks, the sample and type of imaging required determine which of these techniques is most useful. The basic

To be published in Magnetic Imaging and its Applications to Materials

features of most of these techniques have been compared in several recent reviews [12, 13, 14, 15]. SEMPA is particularly well suited for the high resolution imaging of magnetic structures at surfaces and in thin films. For these samples, SEMPA can provide a direct picture of the magnitude and direction of the magnetization (not magnetic field) that is inherently independent of the topography. Moreover this imaging is done with the high spatial resolution, the large depth of field, and the ease of use of the SEM.

The purpose of this review is to present a brief overview of the technique and to describe the types of magnetic imaging applications for which SEMPA is best suited. The origin of the magnetic contrast will be described as well as the instrumentation required for its measurement. The review will highlight SEMPA characteristics by presenting a sampling of recent examples of SEMPA imaging.

6.2 Spin Polarized Secondary Electron Magnetic Contrast

The magnetic contrast in SEMPA is due to the spin polarization of secondary electrons emitted from a magnetic sample. This polarization is related directly to the net spin density and hence the magnetization of the sample. For simple transition metal ferromagnets this polarization can be quite large and, combined with the fact that a large number of secondary electrons are produced in an SEM, the raw magnetic signal in a SEMPA measurement can be quite substantial.

The electron spin contribution to the magnetization is

$$M = -\mu_B (n_\uparrow - n_\downarrow)$$

where $n\uparrow$ ($n\downarrow$) are the number of spins per unit volume that are aligned parallel (antiparallel) to the magnetization, and μ_B is a Bohr magneton. The minus sign results from the fact that the magnetic moment of the electron is directed opposite to its spin. For transition metal ferromagnets, such as Fe, Co, or Ni, in which the orbital moment is quenched, this spin contribution to the magnetization is a close approximation to the total magnetization.

The spin polarization of the emitted secondary electrons directly probes the spin part of the magnetization. Since the electrons retain their spin orientation during the emission process, the secondary polarization is along the same direction as the magnetization. The spin polarization, like the magnetization, is a vector quantity. For the

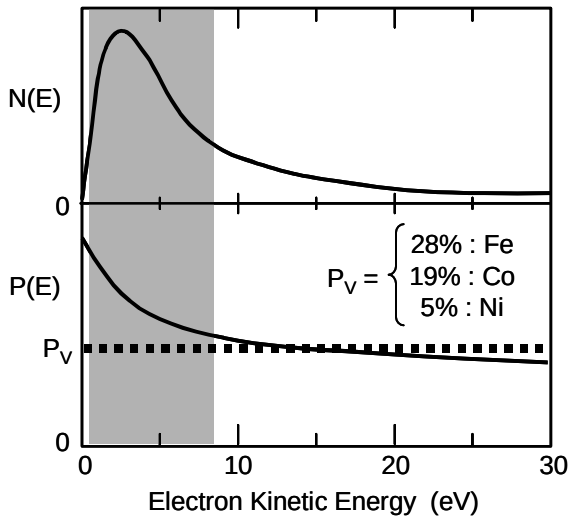

Fig. 6.1 Schematic energy distribution of the number, *N(E)*, and polarization, *P(E)*, of secondary electrons emitted from a typical transition metal ferromagnet. The shading highlights the approximate energy range accepted by the polarization analyzer used in the SEMPA measurements.

purposes of SEMPA it is adequate to consider each component of the polarization separately. For example, the polarization along the *z* direction is

$$P_z = \frac{(N_\uparrow - N_\downarrow)}{(N_\uparrow + N_\downarrow)}$$

where $N\uparrow$ ($N\downarrow$) are the number of electrons with spins parallel (antiparallel) to the $+z$ direction. Note that the polarization is independent of the total number of electrons and that it may have values $-1 \le P \le 1$.

A sketch of the typical energy distribution of the polarization, *P(E)*, and the number, *N(E)*, of secondary electrons emitted from a ferromagnet is shown in Fig. 6.1. The secondary electron intensity distribution shows the familiar peak at low energies due to the secondary electron cascade process. The total secondary electron yield is on the order of 10% of the incident electron beam current and depends sensitively on the sample and the incident beam energy and angle. On the other hand, the polarization is relatively insensitive to the incident beam conditions. The low energy cascade electrons are the result of electron-hole pair excitations in the valence band. To the extent that the electron cascade represents the uniform excitation of electrons from the valence band, the expected polarization is

$$P(E) = \frac{n_B}{n_V}$$

where n_V is the number of valence electrons per atom, and n_B is the number of Bohr magnetons per atom. The number of Bohr magnetons equals the difference between the number of majority spin and minority spin electrons per atom. For Fe, Co, and Ni this simple model predicts polarizations of 28%, 19%, and 5%, respectively. These values agree well with measured polarizations for secondary electron energies between 10 and 20 eV for Fe [16], Co [16], and Ni[17]. At energies below 10 eV, the secondary polarization increases from the predicted values. This enhancement is the result of spin dependent filtering of the lowest energy electrons [18, 19]. Minority spin electrons are more likely to be lost from the secondary distribution, because in a ferromagnet there are more empty minority states than majority states available for the electrons to decay into before emission.

Although the secondary electron polarization is directly proportional to the magnetization, in practice, the constant of proportionality may be difficult to determine. In general, the energy dependence of the polarization for a particular sample composition may not be known, and the range of secondary electron energies accepted by a polarization analyzer may not be well defined. In general, SEMPA can therefore directly measure the magnetization direction and relative magnitude of the magnetization, but it usually is not possible to determine the absolute value of the magnetization.

A final important feature of the secondary electrons is their short mean free path in the solid. While the energy of the incident electron beam is deposited several hundred nanometers into the sample, the mean free path of the low energy secondary electrons is only on the order of a nanometer. For spin polarized secondary electrons the 1/*e* sampling depth, or average spin attenuation length, ranges from 0.5 nm for a transition metal like Cr [20] to about 1.5 nm for a noble metal like Ag [21]. The effective probing depth of SEMPA is therefore about one nanometer. The combination of shallow probing depth and small beam diameter means that very little magnetic material is required for a SEMPA measurement. SEMPA can sense the magnetization of as few as a thousand ferromagnetic Fe atoms.

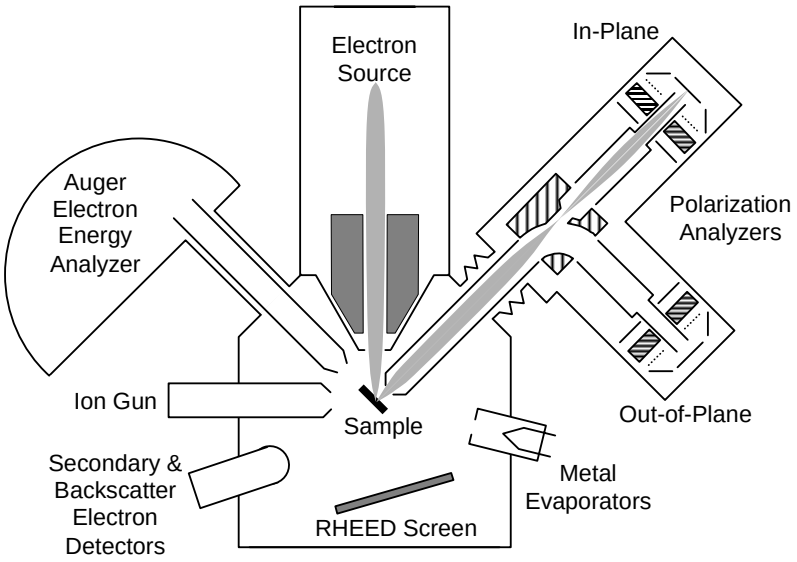

Fig. 6.2 SEMPA apparatus schematic. The incident electron beam, polarization analyzers, and RHEED screen are positioned as shown. The other components are not shown in their true positions.

6.3 Instrumentation

The essential elements of a SEMPA imaging system are: 1) a SEM column to form and raster the incident electron beam, 2) an ultrahigh vacuum chamber with associated instrumentation for surface preparation and surface analysis, 3) spin polarization detectors consisting of electron optics for collecting the secondary electrons and polarization analyzers for measuring their polarization, and 4) a data acquisition system for collecting, storing, and displaying the magnetization images. An overview schematic of our SEMPA apparatus is shown in Fig. 6.2.

6.3.1 Electron Microscope and Specimen Chamber

The spatial resolution of SEMPA is ultimately determined by the size, intensity and stability of the focused incident electron beam. Naturally a small spot size is desirable, but beam intensity and stability are just as important, since the inefficiency of the spin polarization analyzers mandate long exposure times. Furthermore, the working distance between the sample and column must be large enough to allow access to the secondary electrons and minimize the objective lens magnetic field at the sample. Typical operating conditions are: a 10 mm working distance, a stray field at the sample of < 80

To be published in Magnetic Imaging and its Applications to Materials

A/m (1 Oe), and a 10 keV incident electron beam energy. The best SEMPA resolution so far is about 20 nm and has been achieved using a high brightness field emission electron source [22]. Most of the images presented here have been obtained using a LaB_6 thermionic emission cathode which provides 50 nm resolution in a reasonable (< 1 hour) acquisition time. With recent improvements to commercial field emission SEMs it should be possible to obtain ≤ 10 nm SEMPA resolution.

The choice of electron microscope and specimen chamber are further constrained by the surface sensitivity of SEMPA. An ultrahigh vacuum surface analysis environment is required. The vacuum should be better than 10^{-7} Pa to avoid sample contamination that could significantly diminish the magnetic contrast. Conventional surface science preparation techniques such as ion sputtering and annealing, and surface analysis techniques such as Auger spectroscopy, to measure the surface chemical composition, are desirable. Such requirements are conveniently met by commercial scanning Auger microprobes such as the one shown in Fig. 6.2. This apparatus has a hemispherical energy analyzer for Auger analysis, a phosphor screen and electron multiplier for reflection high energy electron diffraction (RHEED) measurements of surface and thin film atomic scale order, and various evaporators for growing thin films. The sample is mounted on a high stability stage which allows heating to 800°C and optional liquid nitrogen cooling. A great advantage of such a system is that sample preparation and analysis can all be done completely *in situ.* In fact, SEMPA imaging can be used to continuously monitor the magnetic structure during the entire sample preparation process.

6.3.2 Spin Polarization Analysis

The spin polarization detectors consist of an electron optical system for collecting the emitted secondary electrons, and one or more spin polarization analyzers for measuring the various components of the polarization vector. In our SEMPA apparatus a +1500 V bias is applied to the front of the transport optics and it is brought to within 12 mm of the sample. This bias voltage helps collect most of the secondaries and accelerates them so that they spend less time in the potentially depolarizing stray magnetic fields of the sample and objective lens. The transport optics are designed to transmit nearly all secondary electrons with an initial kinetic energy between 0 and 8 eV to the spin analyzer. The transport optics also contain electrostatic deflection plates that center the

beam in the polarization analyzer and keep the beam stationary at the analyzer while the incident beam is scanned across the sample. Without these descan optics the beam motion during large area scans could introduce instrumental artifacts in the SEMPA images. As seen in Fig. 6.2, the transport optics also contain a 90° spherical deflector to switch the beam between two orthogonal spin analyzers. Two analyzers are required to completely resolve all of the components of the magnetization vector, since a single detector can only measure two transverse polarization components. In our geometry, one detector measures the two in-plane magnetization components, while the second measures the out-of plane component along with a redundant in-plane component which is useful for cross calibration of the analyzers. Alternatively, all three magnetization components can be measured using a single detector along with a polarization rotator [23, 24].

The key element of the SEMPA apparatus is the spin polarization analyzer. The characteristics of various spin analyzers have been compared [25, 26], and the application of some of them to SEMPA has been discussed [10, 27]. Unfortunately, although several different types of analyzers are available, they all share the common characteristic of very low efficiency. The most efficient spin analyzers have a figure of merit of about 10^{-4}. This means that a polarization measurement will take 10^4 times longer to achieve the same signal-to-noise as an intensity measurement which has nearly 100 % efficiency. The data acquisition rate in SEMPA imaging is therefore limited much more by the detector than the secondary electron signal. In other words, if more efficient spin polarization analyzers could be found, SEMPA could image magnetic structure nearly as fast as a SEM images topography.

Most commonly used spin analyzers rely on the asymmetry of spin-orbit scattering as the basis of their spin sensitivity. Figure 6.3 shows a schematic of our spin analyzer. It is a low energy diffuse scattering analyzer in which the polarized electrons with 150 eV of kinetic energy are scattered from an amorphous Au film [25, 28]. The polarized electrons are scattered diffusely by the Au target and are then deflected by the electrodes E1 and E2 so that their trajectories are approximately normal to grids G1 and G2, which filter out the low energy inelastically scattered electrons from the Au target. The remaining electrons are amplified by the microchannel plates and then collected by

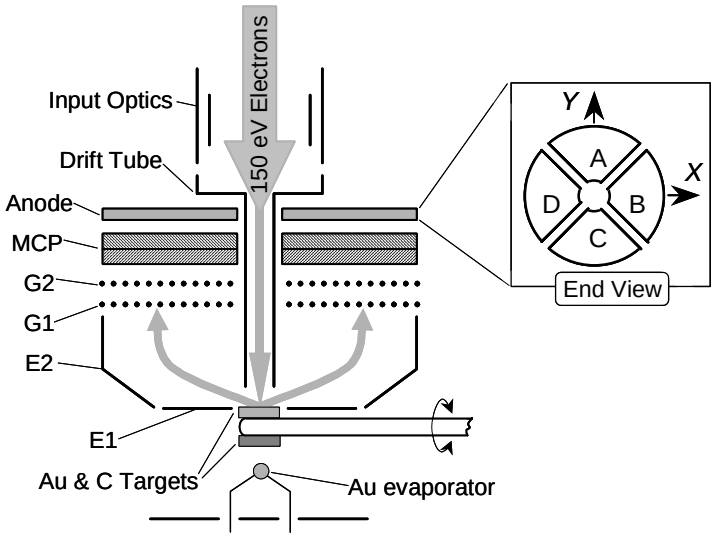

Fig. 6.3 Cross-sectional schematic of a low energy diffuse scattering polarization analyzer. Inset shows the split quadrant anode arrangement.

the four quadrant anode shown in the inset of Fig. 6.3. Two orthogonal components of the transverse polarization are measured simultaneously:

$$P_x = \frac{1}{S}\frac{\left(N_C - N_A\right)}{\left(N_C + N_A\right)}$$

and

$$P_y = \frac{1}{S}\frac{\left(N_B - N_D\right)}{\left(N_B + N_D\right)}$$

where N_i is the number of electrons counted in quadrant i, and S is the instrumental Sherman function. The Sherman function is a measure of the spin sensitivity of the detector and is equal to the measured, normalized asymmetry for 100% polarized incident electrons. The overall efficiency of the analyzer is given by the figure of merit,

$$F = S^2\left(\frac{I}{I_o}\right)$$

where I_o is the incident beam current, and I is the current reflected from the Au target. For this analyzer, $S = 0.10$ and $I/I_o = 2\times10^{-2}$, so that the efficiency is 2×10^{-4}.

The low energy diffuse scattering detector has several characteristics that are desirable for SEMPA imaging. First, the detector is sufficiently compact and robust so that it can be added to the electron microscope without adversely affecting the operation

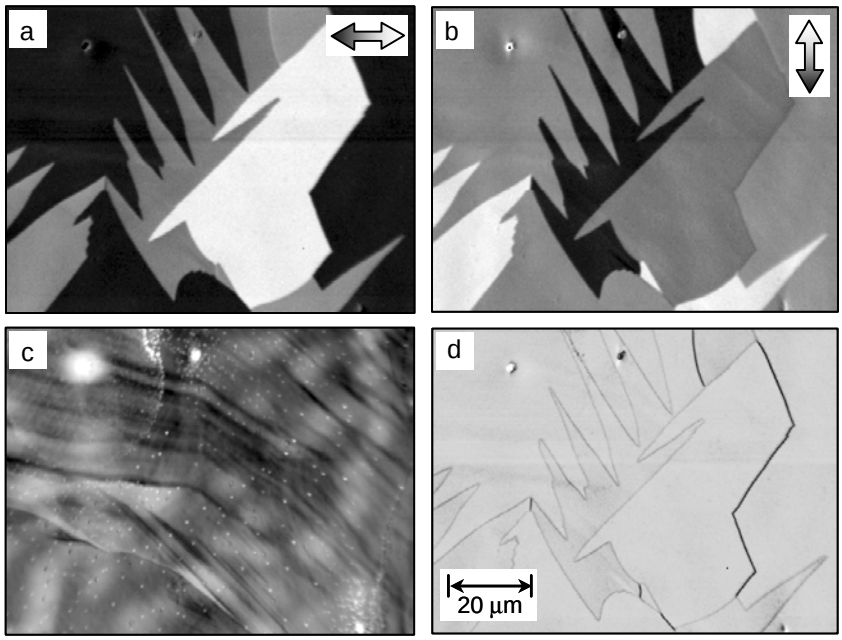

Fig. 6.4 SEMPA measurement example from a recrystallized Fe(100) sample. The in-plane (a) horizontal, and (b) vertical magnetizations, as well as (c) the topography, were measured simultaneously. (d) The derived magnitude of the magnetization. The derived magnetization angle is shown in color Fig. 6.16 (a).

of either the detector or the SEM. Second, the relatively high efficiency is almost constant over the 8 eV energy spread of the incident electrons. Third, the electron optical phase space acceptance of the detector is large enough to collect most of the secondary electrons. Note that other spin analyzers have also been successfully used for SEMPA imaging and can offer other features that may be desirable in particular applications [10].

6.3.3 SEMPA Imaging Example

An example of a SEMPA measurement is shown in Fig. 6.4. The sample is nominally the (100) surface of a Fe crystal, but the surface has been roughened by momentarily heating the sample above the bcc to fcc phase transition at 910 °C. The simultaneously measured in-plane magnetization components, M_x and M_y, and topography, I, are shown in Fig. 6.4 (a), (b), and (c), respectively. The detector axes are approximately aligned with the in-plane (100) easy axis directions. Figure 6.4 (a) is therefore sensitive to magnetic domains that point to the right (white contrast) and left (black), while Fig. 6.4 (b) is sensitive to domains that either point up (white) or down (black) relative to and in the plane of the page. Note that, aside from a few nonmagnetic

defects, the topography is essentially absent from the magnetization images. From the two components of the magnetization, the direction, θ, and magnitude, $|M|$, of the resultant magnetization vector can be simply derived,

$$|M| = \sqrt{M_x^{\,2} + M_y^{\,2}} \qquad \text{and} \qquad \theta = \tan^{-1}(M_y / M_x) .$$

The magnitude is displayed in Fig. 6.4 (d). As expected $|M|$ is constant except for the nonmagnetic defects and some missing magnetization at the domain walls. The missing magnetization at the domain walls is due to averaging the magnetization from adjacent domains with an electron probe diameter that is comparable to the domain wall width. This also explains why the 180° walls appear darker than the 90° walls. Smaller probe diameters can be used to resolve the internal structure of the domain walls, and , in particular, the unique structure of the walls at the sample surface [29, 30, 31].

The direction of the magnetization derived from the images in Fig. 6.4 is shown in the color image in Fig. 6.16 (a). In this image color is used to represent the direction of the magnetization. A color wheel inset in the image provides the key for mapping color into direction.

6.3.4 Instrumental asymmetries

A common problem with spin analyzers is the elimination of false polarization signals due to instrumental asymmetries. Constant polarization offsets, such as those due to mechanical misalignment or unbalanced electronic gains in the different channels, can be measured and accounted for in a reasonably straight forward way. More troubling are asymmetries resulting from changes in the position or the angle of incidence of electrons at the spin analyzer target. For example, the electron beam at the analyzer target may move as the incident electron beam is scanned over the sample. This false asymmetry can be minimized by descan deflection plates in the transport optics.

The sample may also introduce instrumental asymmetries. The application of an extraction voltage makes the sample part of the electron optics and therefore the electron trajectories may be influenced by the geometry of the sample and sample holder. Variations in a sample's work function, stray magnetic fields, and topography may also introduce false asymmetries. These instrumental affects may be reduced by designing the input electron optics such that beam displacements cause compensating changes in the

incident angle at the analyzer target [28]. Instrumental effects can also be minimized by using high voltage Mott spin analyzers which have a greater electron optical phase space acceptance.

In cases where the sample geometry deviates significantly from planar, such as spheroidal or wire samples, the secondary electron trajectories can be sufficiently disturbed that topographic features are visible in the polarization image. In such cases, a non-magnetic reference image can be used to remove the topographic contrast. In the analyzer shown in Fig. 6.3 this is accomplished by replacing the Au target with a low atomic number graphite target. A reference image is then acquired that only shows the non-magnetic signal and not the spin dependent contribution. The graphite target image is then subtracted from the Au target image to obtain the magnetization image [8].

6.3.5 Acquisition Time

The time required to acquire a SEMPA image with a given signal to noise ratio, and the spatial resolution of the image are closely coupled, since the incident electron beam current of the SEM decreases rapidly as the spot size is reduced. The signal to noise ratio, *SNR*, of a measurement of the polarization, *P*, after counting *N* electrons and using a detector with a figure of merit, *F*, is

$$SNR \equiv \frac{P}{\Delta P} = P\left(NF\right)^{1/2}.$$

The number of electrons that arrive at the detector during a time, τ, is

$$N = \delta_{se}\eta I_p \tau / e,$$

where δ_{se} is the secondary electron yield, η is the collection and transport efficiency of the polarization detector input optics, I_p is the beam current incident on the sample, and e is the electron charge. Assuming perfectly efficient electron counting, the total time required to acquire a SEMPA image consisting of n_{pix} pixels is then

$$T = \frac{n_{pix}\left(SNR\right)^2 e}{P^2 F \delta_{se}\eta I_p} = C\frac{n_{pix}\left(SNR\right)^2}{I_p},$$

where C is a number that combines all of the instrumental and sample dependent quantities. For our spin polarization optics and detector, we measure $C=2.0\pm0.5\times10^{-13}$A·s using a 10 keV incident beam and a clean Fe sample.

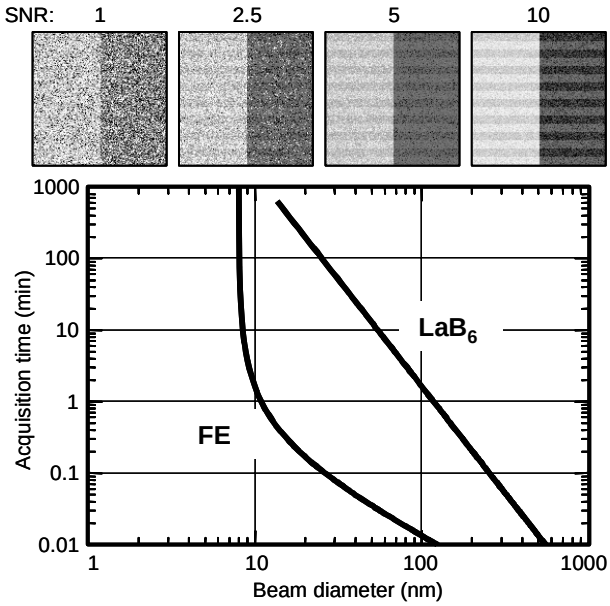

Fig. 6.5 Simulated SEMPA images with different signal to noise ratios, *SNR*, are shown across the top. Simulated magnetic structure in the images is a 180 ° Fe domain wall with superimposed ± 5 ° "ripple". The acquisition time for a 128 × 128 pixel SEMPA image of Fe with *SNR*=5 is plotted below as a function of incident electron beam diameter for LaB_6 and thermally assisted field emission electron sources.

The spatial resolution is ultimately determined by the incident electron beam diameter, which decreases with decreasing beam current, I_p, in a manner that depends on the specific electron source and probe forming optics. Figure 6.5 shows the relationship between image acquisition time and resolution for two electron microscope columns; one using a thermal LaB_6 source and the other using a thermally assisted field emission source. These calculations use the measured dependence between I_p and beam diameter for 10 keV incident beam energies and a 10 mm working distance. These acquisition times are for a 128×128 pixel image of Fe with a *SNR* of 5.

A series of simulated SEMPA images across the top of Fig. 6.5 demonstrates how the *SNR* affects the image quality. The magnetic structure in the simulated image consists of two oppositely magnetized vertical domains that contain a small, ±5°, periodic "ripple". Although the primary signal, the 180° domain wall, is clearly visible with a *SNR* of one, a *SNR* of at least five is required before the ripple fine structure becomes clearly visible.

From Fig. 6.5 it can be seen that acquisition times can range from less than minutes, to hours. Using a LaB_6 source, a low resolution probe is usually used to quickly survey a sample and find specific regions of interest. Long scans with high resolution probes are then used for higher quality images of small magnetic structures. If the samples have a low spin polarization or more pixels with higher signal to noise ratios are required, high resolution images may take hours to accumulate. In these case, special care must be taken to avoid, or to compensate for slow drifts in the position of the sample or electron source.

Finally, it is worth noting that while the above discussion considered only the image acquisition time for a single polarization component, one other orthogonal polarization component and the topography are measured simultaneously. No additional time is required to acquire these additional images.

6.3.6 Applied magnetic fields

Because SEMPA is an electron beam based technique, imaging cannot easily be carried out in the presence of a large applied magnetic field. A magnetic field cannot only deflect the incident beam and the emitted secondary electron trajectories, but it can also cause the secondary electron spins to precess, thereby distorting and degrading the polarization signal. Of course these effects depend sensitively on the specific orientation of the magnetic field relative to the trajectories and polarization of the electrons, but the magnitude of the effects is roughly the same, i.e., a field which causes a 10° deflection will also cause about a 10° rotation of the polarization.

Usually ambient magnetic fields less than 80 A/m (1 Oe) are not a problem. Larger applied magnetic fields, up to 8 kA/m (100 Oe), have been accommodated using various methods that depend on the specific sample being analyzed. For example, the sample can be made part of a closed loop magnetic circuit, reducing the stray magnetic field [32]. In perpendicularly magnetized samples, the applied field effects can be minimized, since the field, polarization, and some of the secondary electron trajectories are all aligned [11]. Finally, for very small samples, it should be possible to apply very localized magnetic fields, using recording heads, for example, that minimize the exposure of the electrons to the applied field.

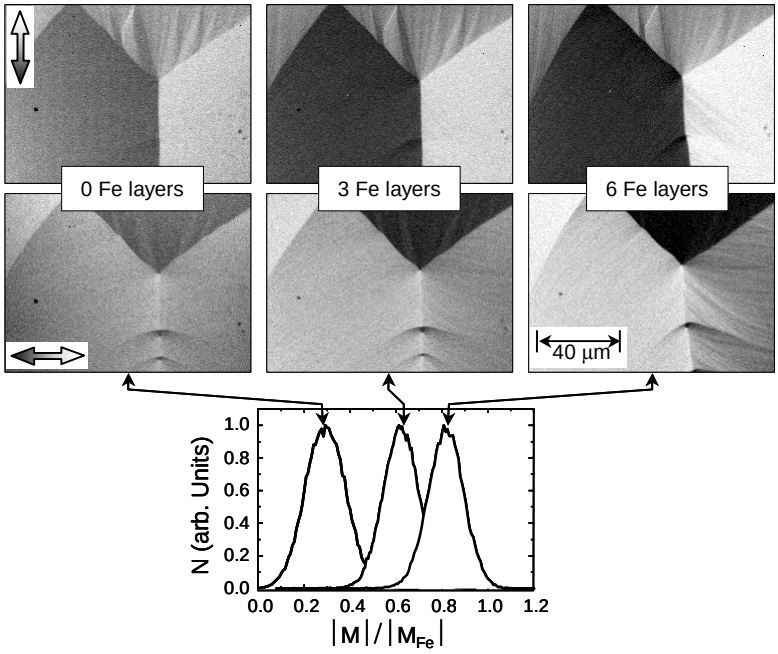

Fig. 6.6 SEMPA images of vertical and horizontal in-plane magnetizations in a permalloy thin film sample, uncoated, and coated with 3 and 6 atomic layers of Fe. Histograms of the corresponding magnetization magnitudes normalized to pure Fe are plotted below.

6.4 Examples of SEMPA Applications

6.4.1 Fe Coatings for Polarization Enhancement

Ultrathin ferromagnetic coatings can occasionally be used to improve the magnetic contrast of samples with inherently low secondary electron spin polarization. For example, Ni or Ni based alloys such as permalloy have relatively weak polarization contrast. Similarily, magnetic materials such as garnets not only have very low secondary electron polarization, but are also insulators. In these cases, one can take advantage of the surface sensitivity of SEMPA and coat the samples with ultrathin films of higher spin polarization materials, usually Fe or Co. In most cases, the magnetic structure of the sample is not appreciably altered, since only a few monolayers of Fe are needed to significantly boost the secondary electron polarization. And, in the case of certain insulators, a few monolayers may also be sufficient to reduce sample charging.

Figure 6.6 shows a series of SEMPA images from the same area of a permalloy sample that is coated with 0, 3, and 6 atomic layers of Fe (0, 0.43 and 0.86 nm thick Fe

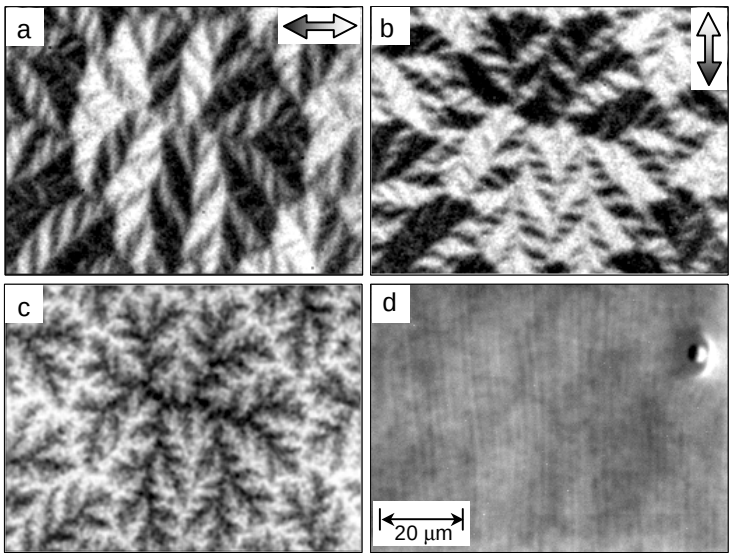

Fig. 6.7 SEMPA images of the in-plane (a) horizontal, (b) vertical, and (c) the out-of-plane magnetization components of a Co(0001) surface domain structure. (d) The simultaneously measured topography. The magnetization direction is shown in color Fig. 6.16 (b).

films). The permalloy sample is a patterned 80 nm thick film with Néel walls that contain cross ties that are visible in the uncoated sample. The images show a dramatic improvement in contrast with just a thin coating of Fe. Details, such as magnetization ripple, that are barely seen in the uncoated sample, are clearly visible in the coated permalloy sample. The improvement in contrast can be made more quantitative by plotting the histograms of the magnetization magnitudes from the three images as shown in the bottom of Fig. 6.6.

6.4.2 Three Dimensional Magnetization Imaging

Complete three dimensional imaging of the magnetization vector is relatively straightforward in SEMPA imaging. An example of a three dimensional magnetic structure imaged using SEMPA is shown in Fig. 6.7. These SEMPA images show the surface magnetic microstructure of a Co crystal. The *hcp* Co crystal has uniaxial crystalline anisotropy with the easy magnetization axis along the *c* axis. SEMPA has been used to investigate the surface domain structure of Co with the *c* axis lying in-plane [33] and normal to the surface plane [34]. In this case the *c* axis is perpendicular to the surface. Although the domains inside the sample bulk are relatively large and aligned along the *c* axis, at the surface the large amount of magnetostatic energy associated with a

perpendicular component of surface magnetization favors the formation of a complex closure domain structure with a substantial in-plane magnetization component. Figure 6.7 shows all three magnetization components and the corresponding intensity topograph. The two in-plane components were measured simultaneously, while the out-of-plane component was measured in a separate image. The simultaneously measured topography images were used to align the two polarization measurements. The derived in-plane magnetization direction is shown in the color image in Fig. 6.16 (b).

Although determining the magnetization direction at any point on the sample's surface is a relatively straightforward procedure, displaying this complex three dimensional structure is difficult. In Fig. 6.16 (b) a portion of the in-plane magnetization image has been combined with the out-of-plane component to generate a three dimensional rendering of the magnetization direction with color corresponding to the in-plane magnetization direction and height corresponding to the polar component. This image gives a visual impression of the complex closure domain structure of the Co, where the magnetization points into (out of) the surface in the valleys (hills).

6.4.3 Imaging Rough Surfaces

One major advantage of using an SEM for imaging is the relatively large depth of focus. SEMPA can therefore be used to image the magnetic structure of rough samples with surfaces that have considerable three dimensional topography [10, 11]. Although samples with very nonplanar geometries can disturb the secondary electron extraction field and introduce instrumental artifacts in the images, surfaces that deviate a millimeter or less from a planar geometry are generally tolerated.

An example of SEMPA imaging from a rough surface is presented in Fig. 6.8 which shows images from both sides of a melt spun amorphous ferromagnetic glass ribbon. Color images of the magnetization direction are shown in Fig. 17 (a). The as-cast ribbon has a smooth side (the air side) and an optically matte, rough side (the wheel side). The wheel side reflects the roughness of the cooling wheel and includes many voids due to trapped air bubbles. The domain structures of the two sides are very different. The air side reveals mostly large domains usually attributed to the bulk domain structure. These domains, which are usually long , parallel and aligned with the ribbon axis, are shown in Fig. 6.8 (top) interacting with a dimple in the magnetic ribbon. The presence of such

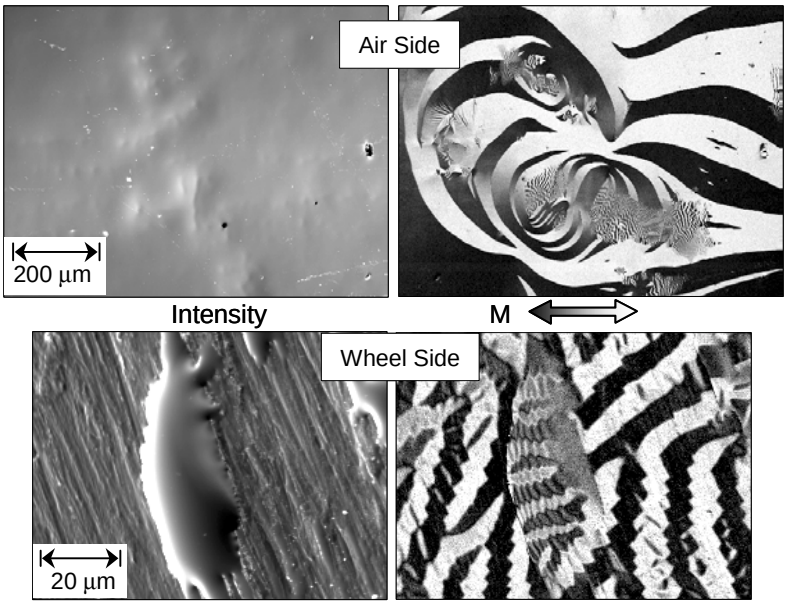

Fig. 6.8 SEMPA images of the topography and horizontal in-plane magnetization component from the smooth, air side and the rough, wheel side of a melt spun ferromagnetic metallic glass ribbon. The magnetization direction images are shown in color Fig. 6.17 (a).

defects can affect the domain wall motion. The ability of SEMPA to acquire simultaneous, yet independent images of the magnetic and topographic structure has been useful for understanding the magnetization dynamics in such a sample [32].

The magnetic structure of the wheel side of the ribbon is much more complex. The magnetization on this side is dominated by fine scale, maze-like domains that are the result of the magnetoelastic response to the strains in this surface. In fact, SEMPA images of similar domain structures have been used to analyze the strain fields in other ferromagnetic glass samples [35]. The large depth of focus allows SEMPA to image the finer domain structure inside the bubble induced pocket as shown in the bottom of Fig. 6.8.

6.4.4 Recording Media

SEMPA has been successfully used to investigate the magnetic structure of hard disk [36, 37] and magneto-optic [38, 39] media. Recently, however, magnetic force microscopy (MFM) has become the more common imaging method for magnetic recording media, to a large extent because it can be performed in air with little or no sample preparation [40]. SEMPA can provide valuable additional information, however,

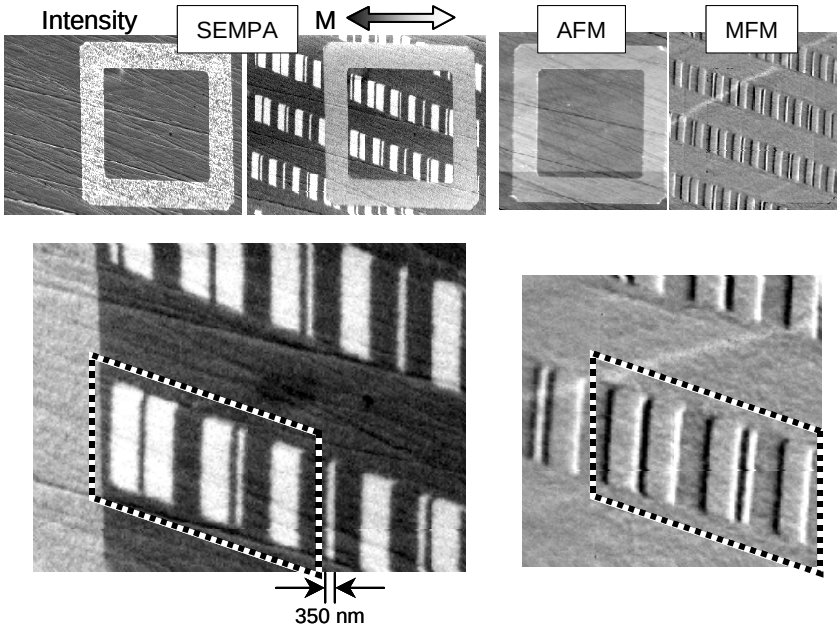

Fig. 6.9 Comparison of SEMPA and MFM images from a thin film hard disc media test sample. Bottom images are magnified views of magnetic structure inside Au box pattern. Dashed boxes outline the same bits in the SEMPA and MFM images. The smallest written bit is 350 nm.

since the two techniques probe different yet complementary aspects of the magnetic structure. SEMPA images the magnetization directly, while the MFM is sensitive to the magnetic fields arising from the magnetization.

SEMPA and MFM images of test patterns recorded in a special thin film media sample [41] are compared in Fig. 6.9. A patterned Au film was deposited on top of the otherwise uncoated magnetic thin film, so that the images could be exactly aligned and the same recorded bits compared. The difference between the magnetic contrast mechanisms of the two techniques is highlighted by two significant differences between the SEMPA and MFM images: First, the magnetic structure underneath the Au film pattern is not visible in SEMPA, but visible with the MFM. SEMPA is more sensitive to the local, surface magnetic structure. And second, since the MFM is sensitive to the gradient of the magnetic field, the strongest MFM contrast occurs at the transitions between the recorded bits. SEMPA, on the other hand, is only sensitive to the magnetization direction. Comparisons such as this have been useful to help understand

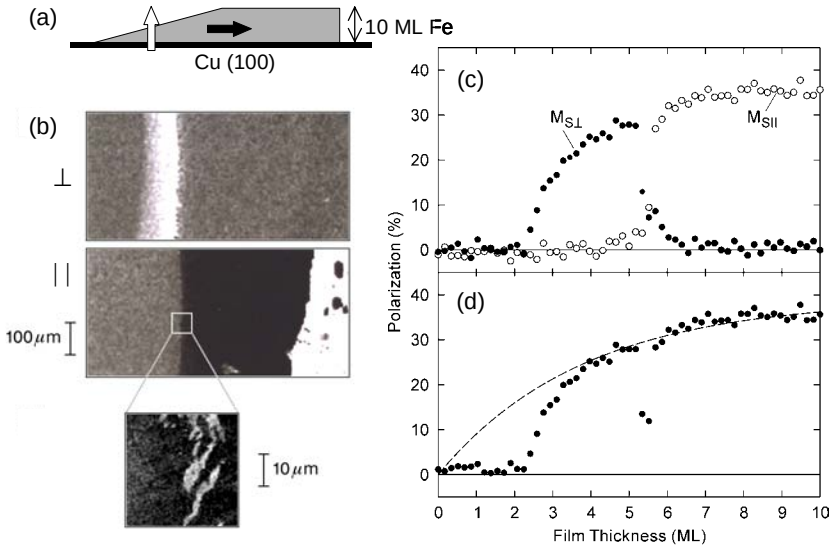

Fig. 6.10 Spin reorientation in Fe/Cu(100) epitaxial films. SEMPA measurements of in-plane and perpendicular magnetization components of a 0 to 10 atomic layer Fe wedge are shown in (b) images, and (c) line scans. Inset shows high resolution image of domain structure near reorientation thickness. (d) Total magnetization. Reprinted with permission from R. Allenspach and A. Bischoff, Phys. Rev. Lett. **69**, 3385-3388 (1992).

the contrast mechanisms in MFM imaging, since the magnetization measured using SEMPA can be used to derive the magnetic fields sensed by the MFM.

6.4.5 Spin Reorientation Transitions

A fruitful area of research exploiting SEMPA's surface sensitivity has involved investigations of spin reorientation transitions in ultrathin magnetic films [42, 43]. In these films, which are only a few atomic layers thick, the magnetization orientation is determined by the balance between surface anisotropy which favors perpendicular magnetization and shape anisotropy which favors in-plane magnetization. Relatively small changes in parameters such as the film thickness, temperature, applied field or chemical composition can alter this balance and change the magnetic orientation between in-plane and perpendicular. SEMPA not only has the surface sensitivity to easily measure the magnetization direction in these films, but SEMPA can also image the domain microstructures which can be quite complex.

An example of such an investigation involves SEMPA measurements of the spin reorientation in epitaxial Fe/Cu(100) films by Allenspach and Bischoff [44]. They

imaged the magnetic structure at several temperatures of a 0 to 10 atomic layer thick wedge of Fe grown on a Cu(100) single crystal substrate. SEMPA images and line scans from a wedge measured at 175 K are shown in Fig. 6.10 (b) and (c), respectively. The magnetic orientation clearly changes from perpendicular to in-plane between a thickness of 5 to 6 atomic layers of Fe. During this transition, very small micrometer sized domains appear as shown in the inset in Fig. 6.10 (b). The presence of these domains could lead a non-imaging magnetization measurement to mistakenly find that the magnetic moment decreases during the transition. In fact, earlier measurements showing reduced magnetizations had led to speculations that the balanced anisotropies at the transition might produce a reduced or paramgnetic Fe moment [45]. The derived magnitude of the magnetization measured by SEMPA shown in Fig. 6.10 (d), however, does not show any reduction in the Fe magnetic moment. Any reduction in the observed magnetization can be accounted for by the finite SEMPA probing depth and a reduced Curie temperature for Fe less than a couple of atomic layers thick. SEMPA images also showed that the domain structures are very sensitive to temperature, varying not only in orientation, but also size and shape as the temperature is varied [44].

6.4.6 Fe/Cr/Fe Exchange Coupling

Advances in thin film growth techniques have lead to an interesting and useful new class of magnetic materials that consist of magnetic multilayers separated by ultrathin nonmagnetic spacer layers [46]. Technologically, these multilayers are significant because they exhibit Giant Magnetoresistance (GMR) effects that occur when the layers are switched from ferromagnetic alignment to antiferromagnetic alignment. This GMR is the basis for various new magnetic sensors and memory devices [47]. Scientifically, these multilayers are interesting because they can exhibit unusual long range oscillatory exchange coupling between the magnetic layers. This coupling is mediated by the nonmagnetic spacer layers, and the direction of the coupling, whether the layers are ferromagnetically or antiferromagnetically aligned, varies with the thickness of the spacer. The surface sensitivity of SEMPA, along with the ability to prepare and study films *in situ,* have made SEMPA a very useful technique for understanding the origins of this oscillatory exchange coupling. In particular, SEMPA has been very useful for

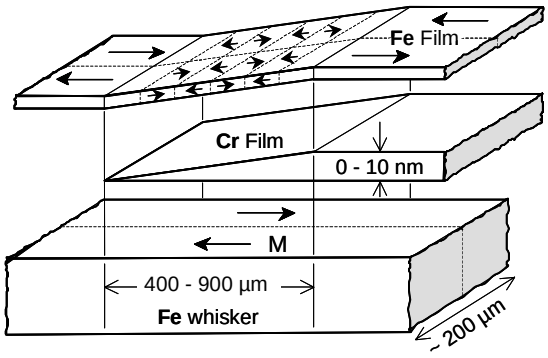

Fig. 6.11 Schematic expanded view of Fe/Cr/Fe exchange coupling sample showing the Fe whisker substrate, the Cr wedge, and the Fe overlayer. Arrows in the Fe correspond to magnetization directions.

measuring how the alignment of the magnetic layers depends on the thickness of the nonmagnetic spacer layer [48, 49].

Several combinations of magnetic and nonmagnetic layers have been investigated using SEMPA, but Fe/Cr multilayers are particularly interesting because the lattices are well matched allowing good epitaxial growth and the Cr can either be in a paramagnetic or antiferromagnetic state [50]. Conceptually, these measurements are relatively simple. The magnetization alignment of the top and bottom ferromagnetic layers of a magnetic sandwich are imaged with SEMPA for various thicknesses of the nonmagnetic spacer. In practice, a great deal of effort goes into finding the optimal conditions for atomically smooth layer-by-layer growth, since roughness as small as a fraction of an atomic layer can significantly affect the coupling. Furthermore, rather than growing and measuring one spacer thickness at a time, the entire thickness dependence of the coupling is measured in a single SEMPA image by preparing samples with variable thickness, wedge-shaped spacer layers.

A schematic of the multilayer sandwich structure used in these measurements is shown in Fig.6.11 . A single crystal Fe whisker is used as the substrate. These whiskers, grown by thermal decomposition of $FeCl_2$ in a H_2 atmosphere, are among the most perfect metal crystals known [51]. More important for thin film growth, nearly perfect (100) surfaces may be obtained by *in situ* ion sputtering of the whisker surface and thermal annealing. Scanning tunneling microscopy (STM) measurements of these

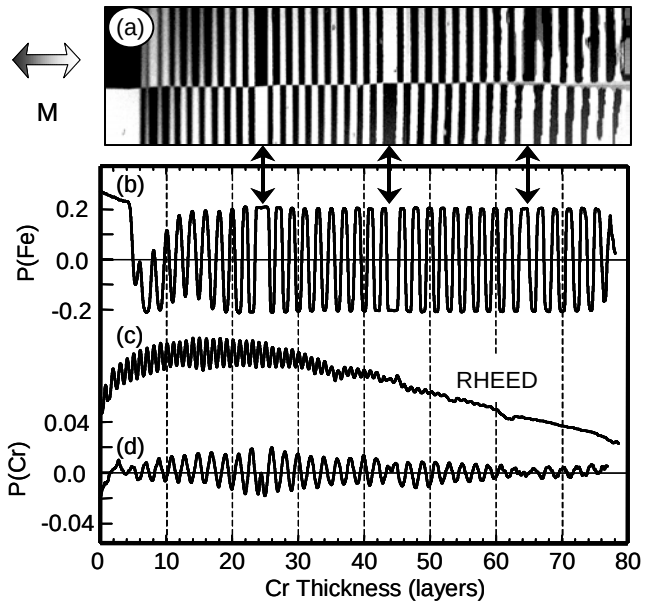

Fig. 6.12 (a) SEMPA image of the Fe overlayer magnetization for the Fe/Cr/Fe wedge structure shown in Fig. 6.11. (b) Line scan of the Fe overlayer magnetization. Arrows point to phase slips in the coupling oscillations. (c) RHEED oscillations from the uncovered Cr wedge used for thickness calibration. (d) Spin polarization of electrons emitted from the uncovered Cr wedge.

surfaces reveal step densities as low as a single atomic step per micrometer [52]. The long whiskers are usually divided into two opposite domains; a useful feature for establishing the zero of the polarization measurement. The Cr wedge is grown by molecular beam epitaxy (MBE) while moving a shutter in front of the whisker. The first two Cr layers are grown at 100° C to minimize interdiffusion, while the rest of the Cr is grown at 300° C to encourage layer-by-layer growth. The thickness of the wedge is measured using spatially resolved RHEED [53]. Figure 12 (c) shows a line scan from a RHEED image showing oscillations of the specular beam intensity; a sign of nearly layer-by-layer growth. Using the measured RHEED oscillations the Cr thickness at any point along the wedge can be measured to within one tenth of a Cr layer (±0.014 nm). The sample is then coated with a thin epitaxial Fe film and the coupling is determined from the direction of the magnetization in this top layer.

The magnetization of the top Fe film is shown in the SEMPA image in Fig. 6.12 (a). The whisker is split into two opposite domains, so that in the lower half of this SEMPA image white (black) contrast corresponds to ferromagnetic (antiferromagnetic)

alignment of the overlayer magnetization with respect to the whisker substrate, while the opposite is true for the upper half of the whisker. A line scan of the magnetization from the lower half of the whisker is plotted in Fig. 6.12 (b). From this measurement one can see that the coupling oscillates between ferromagnetic and antiferromagnetic with a period of nearly two atomic Cr layers. The period is not exactly two layers, but instead 2.105±0.005 atomic Cr layers. This small incommensurability between the lattice and the magnetic coupling is responsible for the phase slips observed at approximately 24, 44, and 64 layers.

SEMPA also provides information about the antiferromagnetic order of the Cr moments in the uncovered Cr film [20]. Because of the shallow probing depth, the polarization measured by SEMPA from the antiferromagnet does not average to zero, but instead, weighs the polarization of the outermost Cr layer more than the rest of the Cr. A line scan of this bare Cr surface polarization, with the background Fe polarization removed, is shown in Fig. 6.12 (d). The uncovered Cr has the same oscillatory periodicity as the exchange coupled Fe film. This is not surprising, since the incommensurate spin density wave nature of Cr is important in both the Cr antiferromagnetism and the Fe/Cr/Fe exchange coupling [50]. Note, however, that the sign of the polarization is reversed, indicating that antiferromagnetic coupling is favored at the Fe-Cr interface.

The ability to grow atomically well ordered magnetic multilayers and examine them in situ makes SEMPA a valuable tool for understanding the exchange coupling in epitaxially grown magnetic multilayers. Although short period oscillatory effects are present in other measurements they are usually difficult to observe, since average interlayer thickness fluctuations of only a few tenths of an atomic layer can average these fine structures away [54]. SEMPA measurements of these nearly ideal systems have therefore provided meaningful informationabout the origins of the exchange coupling, as well as quantitative tests of theoretical models [55].

6.4.7 Depth Profiling Co/Cu Multilayers Magnetization

Not only can SEMPA be used to investigate interlayer coupling in magnetic multilayers as they are grown, in certain cases SEMPA can be used with ion milling to take apart and depth profile magnetic structures in the same way that ion milling and Auger spectroscopy are used to depth profile chemical structure. Magnetic depth

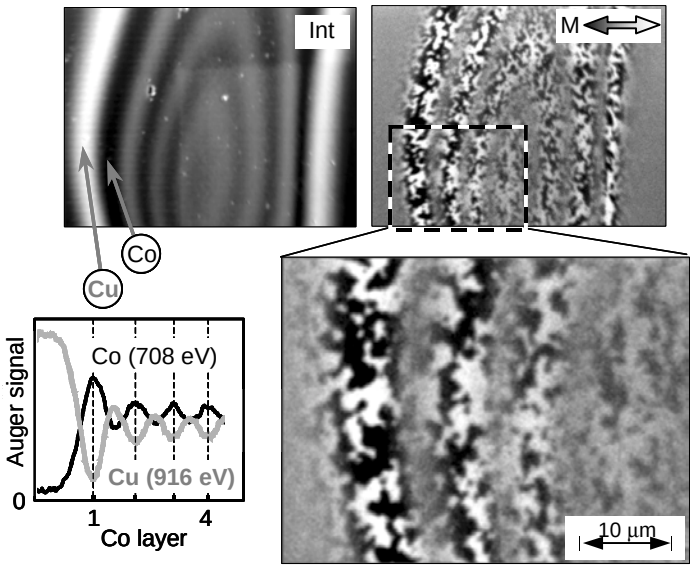

Fig. 6.13 SEMPA images of an ion milled crater in a Co/Cu multilayer. The topography is shown on the left, while the magnetization images on the right shows the magnetic domains in the separate Co layers. The plot shows Auger line scans from one edge of the crater.

profiling works best in weakly coupled magnetic multilayers in which the magnetic structure is pinned in place by some structure in the film. Sputter deposited Co(6nm)/Cu(6nm) multilayers meet these requirements [56]. The 6 nm spacing between magnetic layers insures weak coupling, while the inherent fine scale granularity of a sputter deposited film provides the defect structure for pinning the magnetic structures in place. The outermost magnetic Co layers may therefore be removed by ion milling without significantly disturbing the remaining magnetic structure of the multilayer [57].

The main goal of depth profiling the magnetic structure of the Co/Cu multilayers was to understand how correlations between the domain structure of adjacent layers affect the GMR of these potentially useful sensor materials. Figure 13 shows a test crater ion milled using 2 keV Ar^+ ions into the $[Co(6nm)/Cu(6nm)]_{20}$ multilayer. The SEMPA topography image in Fig. 6.13 show light and dark bands corresponding to the Cu and Co layers, respectively. An Auger line scan taken from one edge of the crater is plotted in Fig. 6.13. Although the Auger depth profile shows some interfacial chemical mixing due to the ion milling, the Co and Cu layers are still clearly differentiated. The SEMPA

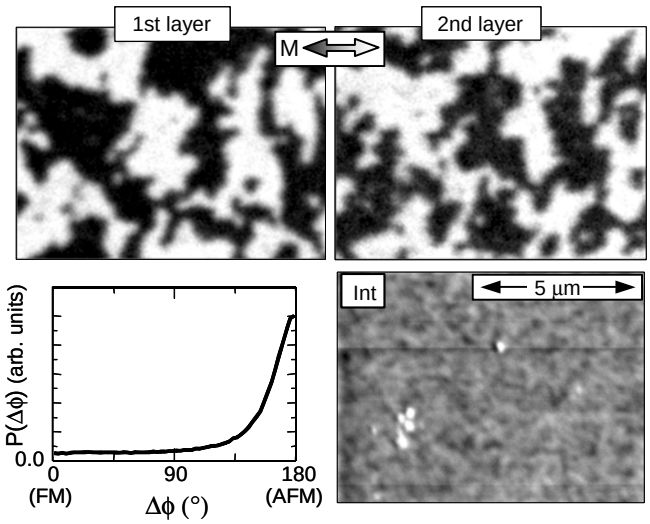

Fig. 6.14 SEMPA images of the outermost two layers of a Co/Cu multilayer exposed by ion milling. The strong anticorrelation of the domain structures is shown in the histogram distribution of the difference in magnetization directions between the two layers. The magnetization directions are shown in color Fig. 6.17 (b).

magnetization images in Fig. 6.13 show that the magnetic domain structure of the adjacent Co layers is also well separated. For this multilayer system, depth profiling could clearly resolve at least the outermost 10 Co layers.

To correlate the magnetic structure in adjacent layers from the same area, the sample was ion milled to a uniform depth over a large part of the sample. Auger spectroscopy was used to determine the depth of the ion milling. SEMPA images from the outermost two Co layers are shown in Figs. 14 and 17 (b). The magnetization images reveal that within the layers the domains have random shapes that are nominally one micrometer in size with uniaxial alignment of the magnetization. As can be seen from the images the magnetization in adjacent layers is strongly anticorrelated. This observation can be made more quantitative by taking the pixel-by-pixel difference of the magnetization direction, $\Delta\phi$, between the two layers. A histogram showing the resulting distribution of alignments is plotted in Fig. 6.14. The plot shows that antiferromagnetic alignment between the adjacent layers is clearly preferred. The antiferromagnetic alignment even extends to structures as small as the domain walls. Within the layers the domain walls are Néel-like with in-plane magnetization and random chirality. Domain

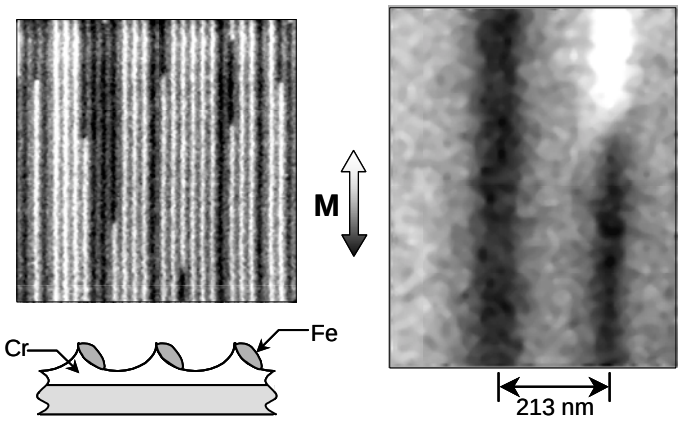

Fig. 6.15 SEMPA images of Fe wires formed by grazing incidence deposition on a Cr grating.

walls in adjacent layers, such as the ones highlighted by the circles in Fig. 6.17 (b), are oppositely magnetized so that the chirality of the walls are the same in the adjacent Co layers. The observed anticorrelations are found to persist for at least the first ten Co layers [57].

The SEMPA measurements of the interlayer magnetic correlations have been used to quantitatively explain the observed GMR in these multilayers [57]. Relative field dependent changes in the GMR are found to be in good agreement with the GMR derived from the SEMPA measured correlations, assuming that the GMR is simply proportional to $-\cos\Delta\phi$. In addition, combining the SEMPA measurements with polarized neutron reflectivity measurements which measure the average magnetic structure has proven to be especially useful for understanding the magnetic structure of these multilayers [58].

6.4.8 Patterned Magnetic Structures

The use of patterned magnetic structures in magnetic technology is ubiquitous. Patterned high density recording media, GMR sensors, and magnetic random access memories (MRAM) are all current examples of magnetic technology where small magnetic structures are important. SEMPA has been used to investigate how the magnetic structure in these systems, or in idealized versions of these systems, is influenced by the shape of the device and the presence of physical or chemical defects.

Figures 6.15 and 6.17 (c) show examples of SEMPA images of patterned magnetic structures with very different length scales. Figure 6.15 shows the domain

structure of very fine Fe wires deposited in situ by grazing incidence evaporation onto a Cr grating [59]. In this case the size and shape of the wires restricts the magnetic structure to single domains with magnetization directions along the length of the wires. Figure 15 also shows a high magnification SEMPA image of the domain transition which is at roughly 45° to the wire.

SEMPA images of much larger lithographically patterned Fe structures are shown in Fig. 6.17 (c). These samples, provided by G. Prinz at the Naval Research Laboratory, consist of Fe films grown epitaxially on GaAs substrates. The patterns are all variations of a rectangular basic shape with sides that are aligned along the (001) easy magnetization axis of Fe. The simplest domain structure for this basic shape would therefore be a "picture frame" structure with a single domain along each side. Instead of this simple domain pattern, however, the structures show what happens to the magnetization when a small gap is introduced in one side of the frame. A more complex structure is formed, allowing the formation of closure domains in the gap which reduce the magnetostatic energy associated with free magnetic poles in the gap. Figure 17 (c) also shows the sensitivity of the domain structures to the size of the structures and to any shaping of corners.

In addition to shape, film thickness can also strongly affect domain structure. This is especially true as the magnetic patterns become nearly two dimensional. The surface sensitivity of SEMPA imaging has made it a useful tool for investigating these systems which can be only a few layers thick. So far the results are somewhat conflicting. For example, for small Co structures grown in situ on Cu(001) substrates, some groups have reported that the magnetic structure is independent of lateral size and shape of structures [60], while others have seen significant dependencies[11]. Clearly, the issue of domain formation in these very small and very thin structures is not as simple as one might anticipate.

6.5 Conclusion

The preceding examples show that SEMPA can be used to image the magnetic microstructure in a wide variety of structures and materials. SEMPA's surface sensitivity

makes it especially well suited for the direct, quantitative mapping of the magnetization direction in thin films and at the surface of magnetic materials. Comparisons between magnetic and physical structure in these systems are facilitated by the natural ability of SEMPA to easily separate the magnetic and topographic contrast. When combined with other compatible surface analytical techniques such a Auger, RHEED and STM, SEMPA can also provide information about the relationship between the magnetic structure, and the chemical structure and atomic scale order.

In the future, advances in electron microscope design should allow the resolution of SEMPA imaging to improve to less than 10 nm. In addition, the development of higher efficiency polarization analyzers could dramatically improve the resolution, as well as the speed of SEMPA. More complex sample holders will also allow the application of localized magnetic fields as well as make simultaneous *in situ* electrical measurements of devices possible. As the lateral size of magnetic structures used in magnetic technologies, such as magnetoelectronics and magnetic storage, continues to shrink from the microscale to the nanoscale, and as the thickness of the magnetic films used in these structures decreases to only a few atomic layers, SEMPA will be ready to provide valuable information about the magnetic microstructure and novel magnetic properties of these systems.

Acknowledgements

I wish to thank my colleagues who have worked with me in developing SEMPA, especially, R. J. Celotta, D. T. Pierce, M. H. Kelley, and M. R. Scheinfein. This work was supported in part by the Office of Naval Research.

Color Plates

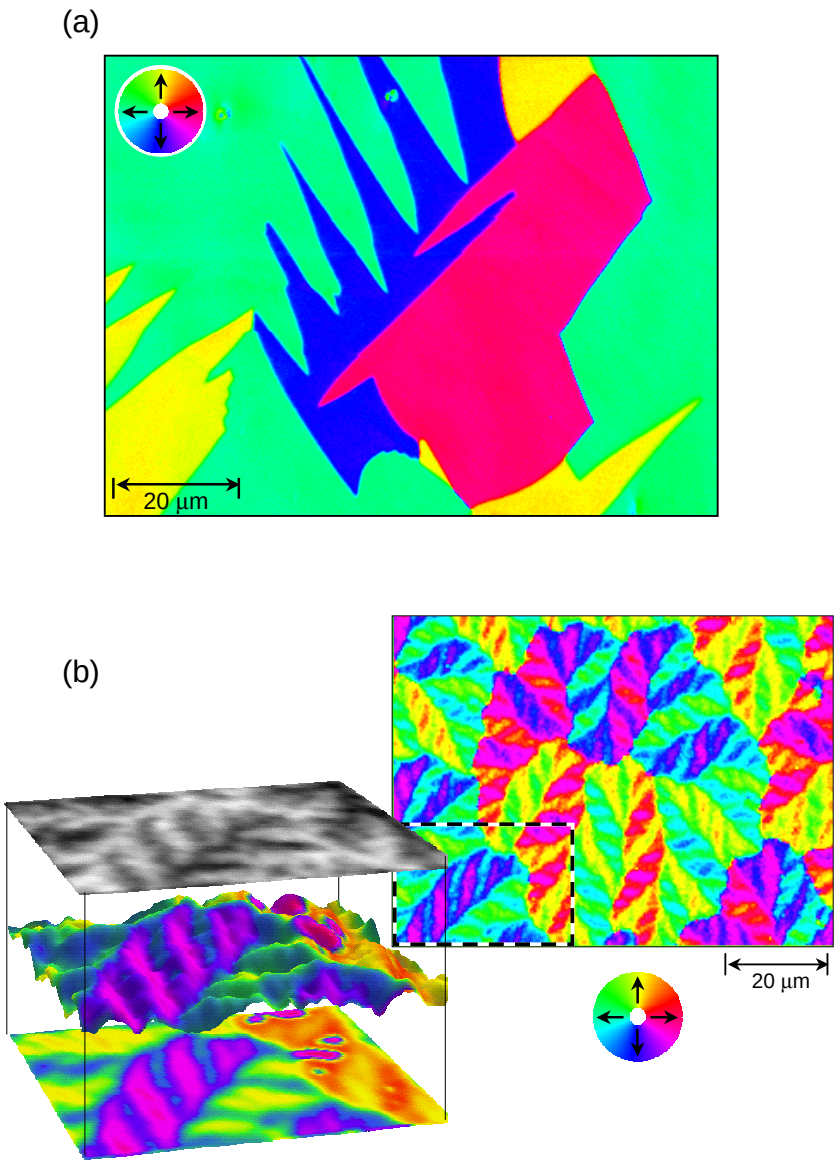

Figs. 6.16 (a) SEMPA image of magnetization direction in Fe(100). Relationship between color and direction is given by colorwheel. (b) In-plane Co(0001) magnetization on right. On the left a boxed portion of in-plane image (shown on the bottom) has been combined with the corresponding perpendicular magnetization image (shown on the top) to generate a three dimensional rendering of magnetization direction (shown in the middle).

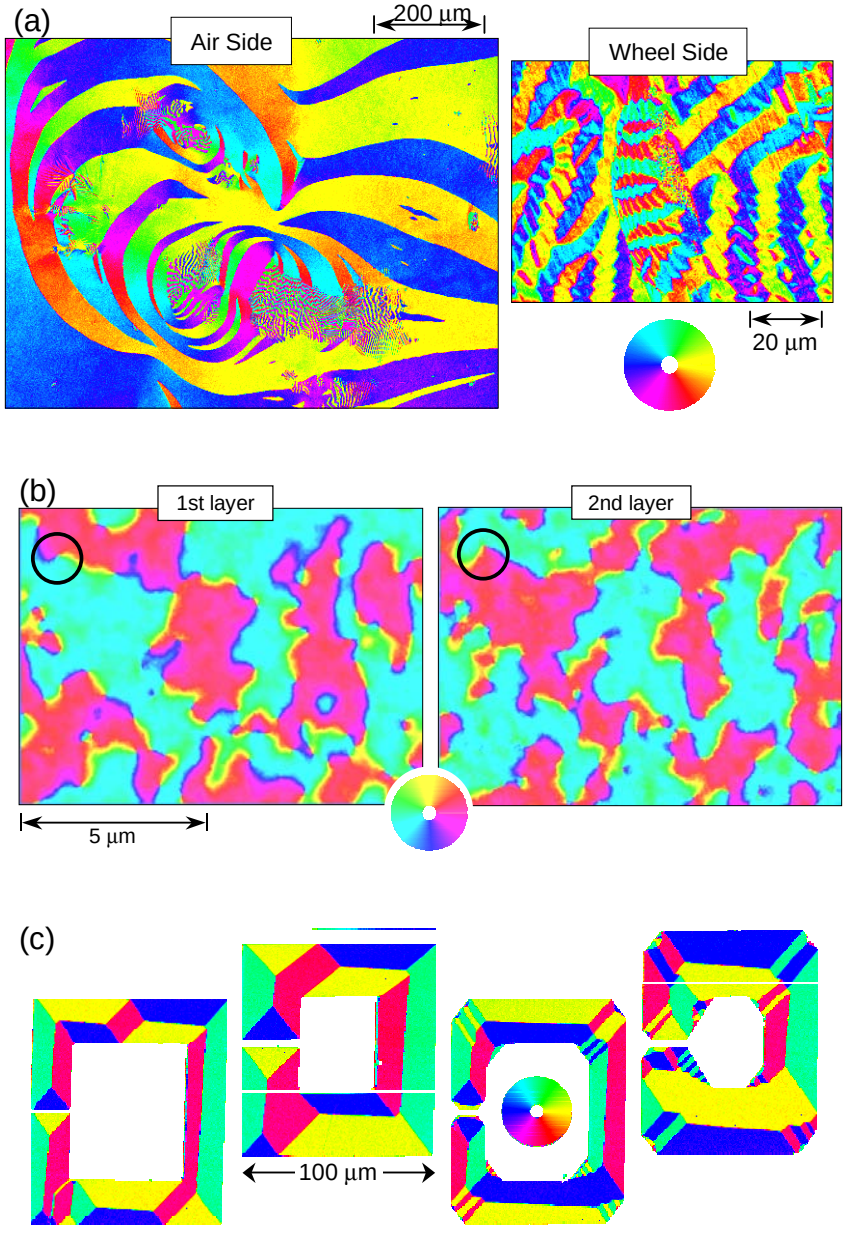

Fig. 6.17 SEMPA images of magnetization direction in (a) an amorphous ribbon, (b) a Co/Cu mulitlayer, and (c) patterned Fe films. Relationship between color and direction is given by colorwheel.

References

1. J. Kessler, 1985, *Polarized Electrons, 2nd Ed.*, Springer, Berlin.

2. R. Feder, 1985, *Polarized Electrons in Surface Physics*, World Scientific, Singapore.

3. R. J. Celotta and D. T. Pierce, Science **234**, 333-340 (1985).

4. J. Kirschner, 1985, *Polarized Electrons at Surfaces*, Springer, Berlin.

5. K. Koike and K. Hayakawa, Jpn. J. Appl. Phys. **23**, L187-L188 (1984).

6. J. Unguris, G. Hembree, R. J. Celotta, and D. T. Pierce, J. Microscopy **139**, RP1-RP2 (1985).

7 H. P. Oepen and J. Kirschner, Scanning Microsc. **5**, 1-16 (1991).

8. J. Unguris, M. R. Scheinfein, R. J. Celotta, and D. T. Pierce, 1990, *Chemistry and Physics of Solid Surfaces VIII, R. Vanselow and R. Howe Eds.*, Springer, Berlin, 239-262 (1990)

9. D. T. Pierce, J. Unguris, and R. J. Celotta, MRS Bulletin XIII (6), 19-23 (1988).

10. M. R. Scheinfein, J. Unguris, M. H. Kelley, D. T. Pierce, and R. J. Celotta, Rev. Sci. Instrum. **61**, 2501-2526 (1990).

11. R. Allenspach, IBM J. Res. Dev., (in press)

12 A. Hubert and R. Schäfer, 1998, *Magnetic Domains: The Analysis of Magnetic Microstructures*, Springer, Berlin.

13 R. J. Celotta, J. Unguris, M. H. Kelley, and D. T. Pierce, *Methods in Materials Research: A Current Protocols Publication, C. L. Chien Ed.*, (Wiley, New York) in press

14 E. D. Dahlberg and R. Proksch, J. Magn. Magn. Mater. **200**, 720-728 (1999).

15 J. N. Chapman and M. R. Scheinfein, J. Magn. Magn. Mater. **200**, 729-740 (1999).

16 E. Kisker, W. Gudat, and K. Schröder, Solid State Commun. **44**, 591-595 (1982).

17 H. Hopster, R. Raue, E. Kisker, G. Guntherodt, and M. Campagna, Phys. Rev. Lett. **50**, 70-73 (1983).

18 D. Penn, S. P. Apell, S. M. Girvin, Phys. Rev. Lett. **55**, 518-521 (1985).

19 D. R. Penn, S. P. Apell, S. M. Girvin, Phys. Rev. B **32**, 7753-7768 (1985).

20 J. Unguris, R. J. Celotta, and D. T. Pierce, Phys. Rev. Lett. **69**, 1125-1128 (1992)

21 J. Unguris, R. J. Celotta, and D. T. Pierce, J. Magn. Magn. Mater. **127**, 205-213 (1993).

22 H. Matsuyama and K. Koike, J. Electron Microsc. (Japan) **43**, 157-163 (1994).

23 M. R. Scheinfein, Optik **82**, 99-113 (1989).

24 T. Kohashi, H. Matsuyama, and K. Koike, Rev. Sci. Instrum. **66**, 5537-5543 (1995).

25 J. Unguris, D. T. Pierce, and R. J. Celotta, Rev. Sci. Instrum. **57**,1314-1323 (1984)

26 D. T. Pierce, M. H. Kelley, R. J. Celotta, and J. Unguris, Nucl. Instrum. Meth. A **266**, 550-559 (1988).

27 J. Barnes, L. Mei, B. M. Lairson, and F. B. Dunning, Rev. Sci. Instrum. **70**, 246-247 (1999).

28 M. R. Scheinfein, D. T. Pierce, J. Unguris, J. J. McClelland, and R. J. Celotta, Rev. Sci. Instrum. **60**, 1-11 (1989).

29 H. P. Oepen and J. Kirschner, Phys. Rev. Lett. **62**, 819-822 (1989).

30 M. R. Scheinfein, J. Unguris, R. J. Celotta, and D. T. Pierce, Phys. Rev. Lett. **63**, 668-671 (1990).

31 M. R. Scheinfein, J. Unguris, J. L. Blue, K. J. Coakley, D. T. Pierce, R. J. Celotta, and P. J. Ryan, Phys. Rev. B **43**, 3395-3422 (1991).

32 A. Gavrin and J. Unguris, J. Magn. Magn. Mater. **213**, in press

33 K. Koike, K. Hayakawa, J. Appl. Phys. **57**, 4244-4248 (1985).

34 J. Unguris, M. R. Scheinfein, D. T. Pierce, and R. J. Celotta, Appl. Phys. Lett. **55**, 2553-2555 (1989).

35 W. J. Tseng, K. Koike, and J. C. M. Li, J. Mater. Res. **8**,775-784 (1993).

36 M. R. Khan, S. Y. Lee, J. L. Pressesky, D. Williams, S. L. Duan, R. D. Fisher, N. Heiman, M. R. Scheinfein, J. Unguris, D. T. Pierce, R. J. Celotta, and D. E. Speliotis, IEEE Trans. Magn. **26**, 2715-2717 (1990).

37 H. Matsuyama, K. Koike, F. Tomiyama,Y. Shiroshi, A. Ishikawa, and H. Aoi, IEEE Trans. Magn. **30**, 1327-1330 (1994).

38 M. Aeschlimann, M. R. Scheinfein, J. Unguris, F. J. A. M. Greidanus, and S. Klahn, J. Appl. Phys. **68**, 4710-4718 (1990).

39 T. Kohashi, H. Matsuyama, Y. Murakami, Y. Tanaka, and H. Awano, Appl. Phys. Lett. **72**, 124-126 (1998).

40 R. D. Gomez, Chap. 3 this book.

41 P. Rice, S. E. Russek, J. Hoinville, and M. H. Kelley, IEEE Trans. Magn **33**, 4065-4067 (1997).

42 W. J. M. de Jonge, P. J. H. Bloemen, and F. J. A. den Broeder, 1994, *Ultrathin Magntic Structures I, J. A. C. Bland and B.Heinrich, Eds.*, (Springer, Berlin), 65-86 (1994).

43 H. P. Oepen, M. Speckman, Y. Millev, and J. Kirschner, Phys. Rev. B **55**, 2752-2755 (1997).

44 R. Allenspach and A. Bischof, Phys. Rev. Lett. **69**, 3385-3388 (1992).

45 D. P. Pappas, C. R. Brundle, and H. Hopster, Phys. Rev. B **45**, 8169-8172 (1992).

46 S. S. P. Parkin, 1994, Ultrathin Magntic Structures II, B.Heinrich and J. A. C. Bland, Eds., (Springer, Berlin),148-185 (1994).

47 G. A. Prinz, J. Magn. Magn. Mater. **200**, 57-68 (1999).

48 J. Unguris, R. J. Celotta, D. A. Tulchinsky, and D. T. Pierce, J. Magn. Magn. Mater. **198-199**, 396-401 (1999).

49 R. Allenspach and W. Weber, IBM J. Res. Dev. **42**, 7-23 (1998).

50 D. T. Pierce, J. Unguris, R. J. Celotta, and M. D. Stiles, J. Magn. Magn. Mater. **200**, 290-321 (1999).

51 A. S. Arrott, B. Heinrich, and S. T. Purcell, 1990, *Kinetics of Ordering and Growth at Surfaces, M. G. Lagally Ed.*, Plenum, New York, 321-341 (1990).

52 J. A. Stroscio and D. T. Pierce, J. Vac. Sci. Technol. B **12**, 1783 (1994)

53 D.T. Pierce, J. Unguris, and R. J. Celotta, 1994, Ultrathin Magntic Structures II, B. Heinrich and J. A. C. Bland, Eds., (Springer, Berlin), 117-148 (1994).

54 D. T. Pierce, J. A. Stroscio, J. Unguris, and R. J. Celotta, Phys. Rev. B **49**, 14564-14572 (1994).

55 M. D. Stiles, J. Magn. Magn. Mater. **200**, 322-337 (1999).

56 W. P. Pratt, Jr., S.-F. Lee, J. M. Slaughter, R. Loloee, P. A. Schroeder and J. Bass, Phys. Rev. Lett. **66**, 3060-3063 (1991).

57 J. Unguris, D. A. Tulchinsky, M. H. Kelley, J. A. Borchers, J. A. Dura, C. F. Majkrzak , Y. Hsu, R. Loloee, W. P. Pratt Jr., and J. Bass, J. App. Phys., in press

58 J. A. Borchers, J. A. Dura, J. Unguris, D. Tulchinsky, M. H. Kelley, C. F. Majkrzak, S. Y. Hsu, R. Loloee, W. P. Pratt Jr., and J. Bass, Phys. Rev. Lett. **82**, 2796-2799 (1999).

59 D. A. Tulchinsky, M. H. Kelley, J. J. McClelland, R. Gupta, and R. J. Celotta, J. Vac. Sci. Technol. A **16**, 1817-1819 (1998).

60 C. Stamm, F. Marty, A. Vaterlaus, V. Welch, S. Egger, U. Maier, U. Ramsperger, H. Fuhrmann, and D. Pescia, Science **282**, 449-451 (1998)